

1     **Defocus and magnification dependent variation of TEM image astigmatism**

2     Rui Yan<sup>a</sup>, Kunpeng Li<sup>a</sup>, Wen Jiang<sup>a,b,c\*</sup>

3     <sup>a</sup>Markey Center for Structural Biology, Department of Biological Sciences, <sup>b</sup>Department of  
4     Chemistry, <sup>c</sup>Purdue Institute of Inflammation, Immunology and Infectious Disease, Purdue  
5     University, West Lafayette, IN 47907, USA

6     \*Corresponding Author:             Wen Jiang

7   Email: [jiang12@purdue.edu](mailto:jiang12@purdue.edu)

8   Tel: 765-496-8436

9

## 10 Abstract

11 Daily alignment of the microscope is a prerequisite to reaching optimal illumination lens and  
 12 imaging lens conditions for high resolution imaging in cryo-EM. In contrast to the dramatic  
 13 progress in automated image acquisition and post-image processing techniques, less attention  
 14 has been paid to the improvement of microscope alignment before data collection. In this  
 15 study, we have employed our recently published tool, *s<sup>2</sup>stigmator*, to study how image  
 16 astigmatism varies with the imaging conditions (e.g. defocus, magnification). We have found  
 17 that the large change of defocus/magnification between visual correction of astigmatism and  
 18 subsequent data collection tasks, or even during data collection will inevitably result in  
 19 undesirable residual astigmatism in the final images. Furthermore, the dependence of  
 20 astigmatism on the imaging conditions varies significantly from time to time, so that it cannot  
 21 be reliably compensated by pre-calibration of the microscope. These findings have essentially  
 22 invalidated a basic assumption of current cryo-EM imaging strategies that assumes invariant  
 23 astigmatism for different defocuses/magnifications used in the microscope alignment stage  
 24 and the final data acquisition stage. Based on these findings, we recommend the same  
 25 magnification and the median defocus of the intended defocus range for final data collection  
 26 are used in the objective lens astigmatism correction task during microscope alignment and in  
 27 the focus mode of the iterative low-dose imaging. It is also desirable to develop a fast,  
 28 accurate method that can perform dynamic correction of the astigmatism for different  
 29 intended defocuses during automated imaging.

30 **Key Words:** defocus-dependent astigmatism; magnification-dependent astigmatism;  
 31 objective lens current; octupole stigmators; vector summation; cryo-EM

32

33

34

## 35 **1. Introduction**

36 Cryo-electron microscopy (cryo-EM) has become a powerful technique for structural studies  
 37 of macromolecular complexes and assemblies at near-atomic resolutions. Good alignment of  
 38 the microscope, such as the gun, condensers, apertures, beam tilt, coma (Ishizuka, 1994;  
 39 Zemlin et al., 1978), astigmatism, *etc.*, is a prerequisite to reaching optimal illumination lens  
 40 and imaging lens conditions for high resolution TEM imaging. Currently, microscope  
 41 alignments are still performed manually and rely on visual, qualitative feedback. Moreover,  
 42 manual microscope alignment requires extensive training and experience but still often suffers  
 43 from suboptimal efficiency and quality. Minimizing astigmatism of the objective lens is an  
 44 indispensable daily instrument alignment task essential for high resolution TEM imaging.

45 Astigmatism of the objective lens represents the angular dependency of defocus. 2-fold  
 46 astigmatism is the major type of astigmatism relevant to cryo-EM, which results in the  
 47 elliptical elongation of Thon rings (Thon, 1971) in the power spectra of TEM images.  
 48 Currently, many microscopists follow a common approach (Grassucci et al., 2008; Sun and Li,  
 49 2010) which is to visually correct astigmatism at large magnifications and small defocuses,  
 50 then switch to a drastically different imaging condition to collect data by intentionally varying  
 51 defocus to sample the entire reciprocal space and even-out the zero-nodes of the contrast  
 52 transfer function (CTF) (Cheng et al., 2015; Penczek, 2010; Zhu et al., 1997). The implicit  
 53 assumption for this common strategy is that the astigmatism is invariant to the change of  
 54 magnification and defocus. However, such invariance has not been quantitatively validated,  
 55 and on the contrary, we have now shown in this study that the assumption is incorrect.

56 Due to the poor sensitivity of human eyes, microscopists have to rely on large magnifications  
 57 and small defocuses when they visually examine the roundness of Thon rings in the 2D power  
 58 spectra displayed on a computer screen and iteratively adjust the two objective lens stigmators  
 59 to make the Thon rings as circular as possible. This tedious and subjective method is not only

60 inaccurate and potentially biased by the astigmatism of human eyes, but also hampers the  
 61 systematic quantification of the astigmatism variations for different magnifications/defocuses.  
 62 To overcome this challenge, it is desirable to take advantage of a proper approach which is  
 63 able to sensitively measure and accurately correct astigmatism at any imaging condition.

64 We have recently published a method,  $s^2stigmator$  (Yan et al., 2017), with a single-pass  
 65 tuning strategy, that allows rapid and sensitive detection of astigmatism using TEM live  
 66 images and can reliably and efficiently guide the user to manually adjust the two stigmators to  
 67 correct astigmatism. This exciting method opens up possibilities to minimize astigmatism  
 68 with real-time feedback at a wide range of imaging conditions that are not available by visual  
 69 examination. In this article, we present systematic and quantitative investigations of  
 70 astigmatism dependence on imaging conditions by employing  $s^2stigmator$  to correct  
 71 astigmatism and then varying imaging conditions (defocus, magnification). Underlying  
 72 physical principles are used to interpret the variability of astigmatism and its dependence on  
 73 image conditions. Based on the findings of these studies, several recommendations are  
 74 provided for instrument alignment and data acquisition to help maximally reduce astigmatism  
 75 and improve high resolution imaging.

76

77

## 78 **2. Method**

### 79 **2.1 Experimental cryo-EM datasets for initial test**

80 Our study started with three datasets of experimental cryo-EM micrographs which were  
 81 downloaded from EMPIAR (Iudin et al., 2016) or collected by our own group. The MAVS  
 82 CARD filament dataset (EMPIAR-10014), plasmodium falciparum 80S ribosome dataset  
 83 (EMPIAR-10028), and our own RNA polymerase dataset (unpublished) were acquired using  
 84 a JOEL 2200FS, a FEI POLARA and a FEI Titan Krios microscope at a nominal  
 85 magnification of 60,000X, 78,000X and 22,500X, respectively. For each dataset, defocus and  
 86 astigmatism were estimated using *ctffind3* (Mindell and Grigorieff, 2003) in order to examine  
 87 the correlation between them.

### 88 **2.2 Data collection for the study of defocus-dependent astigmatism**

89 Next, the defocus-dependence of astigmatism was examined using live images of carbon film  
 90 obtained on our CM200 microscope at 200 kV and FEI Titan Krios at 300 kV, and recorded  
 91 on a Gatan US4000 CCD and K2 Summit camera, respectively. We minimized the objective  
 92 lens astigmatism at small, medium and large defoci using our  $s^2stigmator$  tool, then  
 93 increased or decreased defocus from the starting defocus used for astigmatism correction. At  
 94 each defocus, ten images were collected and their defoci, astigmatisms were calculated to  
 95 obtain their mean and root-mean-square deviation (RMSD) values. The same experiment was  
 96 repeated on different days to explore the reproducibility of defocus-dependence of  
 97 astigmatism.

### 98 **2.3 Data collection for the study of magnification-dependent astigmatism**

99 Finally, the magnification-dependence of astigmatism was examined using the same sample  
 100 and instrument as described above. In order to emulate the change of magnification between  
 101 astigmatism correction and data collection, we minimized the astigmatism at a high

102 magnification using  $s^2$ stigmator, then successively lowered the magnifications. At each  
 103 magnification, twenty images were collected, and their mean and RMSD of astigmatism and  
 104 defocus were computed. In addition to the magnification-dependence of astigmatism,  
 105 magnification-dependence of defocus was also simultaneously examined using the same set  
 106 of data. The same measurement was also repeated multiple times in order to detect the  
 107 stability of the relationship between astigmatism and magnification.

108 The magnifications were calibrated using polycrystalline gold sample grids. The anisotropic  
 109 magnification distortion (Grant and Grigorieff, 2015; Yu et al., 2016) was corrected from the  
 110 live images according to the previously determined parameters before the astigmatism was  
 111 calculated.

112

113

114

### 115 **3. Results**

#### 116 **3.1 Observations of defocus-dependent astigmatism in experimental cryo-EM data**

117 To examine the defocus-dependence of objective lens astigmatism, we first calculated the  
 118 defocus and astigmatism of three cryo-EM datasets as described in Section 2.1 and plotted the  
 119 results in Fig. 1. It can be seen that there are positive correlations between astigmatism and  
 120 defocus, providing evidence for defocus-dependent astigmatism in experimental cryo-EM  
 121 data. It is worth pointing out that this correlation is a general phenomenon since it is observed  
 122 in a wide variety of data, such as data from multiple research groups, different vendors'  
 123 instruments, a diversity of samples, and varying imaging conditions. In our own Titan Krios  
 124 data (Fig. 1C), the astigmatism was calculated after correction of anisotropic magnification  
 125 distortion (Grant and Grigorieff, 2015; Yu et al., 2016). The anisotropic magnification  
 126 distortion in the other two EMPIAR (Iudin et al., 2016) datasets (Fig. 1A, B) was not  
 127 corrected as the distortion parameters were not known. However, these two datasets were  
 128 both imaged at high magnifications in which distortion is generally negligible. As illustrated  
 129 in Fig. 1, the variations of astigmatism for different defocuses are significant (e.g. >100 nm)  
 130 and distinct from dataset to dataset. Hence, it is desirable to comprehensively examine the  
 131 dependence of astigmatism on imaging conditions (e.g. defocus, magnification) which are  
 132 frequently changed in TEM alignment and during data acquisition.

#### 133 **3.2 Robust performance of $s^2$ stigmator and the single-pass tuning strategy at different** 134 **defocuses and magnifications**

135 For quantitative measurement of astigmatism variations, astigmatism needs to be accurately  
 136 corrected at a wide range of imaging conditions, which is very challenging for the current  
 137 method relying on visual examination. We have recently published a closed-form algorithm,  
 138  $s^2$ stigmator, with a single-pass tuning strategy (Yan et al., 2017), that allows fast and sensitive  
 139 detection of astigmatism using TEM live images and guides the users to reliably and

efficiently adjust the two objective lens stigmators to correct astigmatism. Fig. 2 displays two screenshots of the entire trajectories acquired from astigmatism correction processes on Titan Krios (Fig. 2A) and CM200 microscopes (Fig. 2B), respectively. The gray level of the points is varied to make more recent ones darker in order to clearly display the sequence of the points. The user would first adjust either of the two stigmators to find the optimal value (points marked by blue arrows in Fig. 2) that gives rise to minimal astigmatism in the arc-shaped trajectory; then adjust the other stigmator to linearly move the points to the center at which the astigmatism is 0. Thus,  $s^2$ stigmator was used in this study for real-time determination and minimization of astigmatism for systematic studies of objective lens astigmatism.

Next, we tested the performance of our  $s^2$ stigmator method by correcting astigmatism at various imaging conditions, including defocus and magnification. Fig. S1 shows the screenshots of trajectories obtained from Titan Krios when correcting astigmatism at different defoci (Fig. S1A-C) and different magnifications (Fig. S1D-F). In these six screenshots, the trajectories are very similar and all consistently led to correction of astigmatism at a wide range of defoci and magnifications. The angle of the straight trace segment corresponds to the 2nd stigmator used in this single-pass strategy, i.e. stigmator MX in Fig. S1. This angle is determined by the angular position of the stigmators, e.g. octupole objective lens stigmator (Hawkes, 2013; Rai-Choudhury, 1997). Fig. S2 shows the trajectories acquired at a variety of defoci (Fig. S2A-C) and magnifications (Fig. S2D-F) on CM200. Similarly, the change of defocus on CM200 in the range of cryo-EM research does not have a significant influence on the shape of the trajectories (Fig. S2A-C). However, the switch of magnification does have an effect on the orientation of the trajectories (Fig. S2D-F). It is noted that the trajectories turn clockwise when magnification increases (Fig. S2D-F), which is consistent with the rotation of real images at the same set of magnifications (Fig. S2G-I). Moreover, the angle changes of the straight trace segments between two adjacent magnifications are  $14^\circ$  ( $65^\circ$  in Fig. S2D v.s.  $51^\circ$  in S2E) and  $26^\circ$  ( $51^\circ$  in Fig. S2E v.s.  $25^\circ$  in S2F), identical to the change of angles



(marked by red dash lines in Fig. S2G-I) among the corresponding real images ( $14^\circ$  between Fig. S2G and S2H,  $26^\circ$  between Fig. S2H and S2I). Thus, we attribute the rotation of trajectories at different magnifications to the imperfect implementation of the rotation-free imaging function on CM200. In contrast, the rotation-free imaging function on Titan Krios is excellent as shown by the absence of rotations of the trajectories in Fig. S1D-F for different magnifications.

### 3.3 Defocus-dependent astigmatism

After confirming that the astigmatism of objective lens could be accurately minimized using *s<sup>2</sup>stigmator*, we systematically investigated the dependence of astigmatism on defocus using live images of carbon film at room temperature. We first corrected the astigmatism at a specific defocus, then measured the astigmatism with all other instrument parameters remaining constant while only the defocus was gradually altered with a fixed step size (e.g. 100 nm). Fig. 3 shows clear correlation between defocus and astigmatism for both Titan Krios (Fig. 3A-D) and CM200 (Fig. 3E-H) microscopes at a nominal magnification of 22,500X and 115,000X, respectively. At each defocus, the point and error bar represent the mean and RMSD of astigmatism from ten images, respectively. When the astigmatism is minimized at small, medium, and large defocus (red, green and blue lines in Fig. 3A, E), astigmatism linearly increases as the defocus is continuously increased/decreased from the starting defocus used for astigmatism correction. Apparently, the slopes of the lines from CM200 (Fig. 3E) are much larger than those from Titan Krios (Fig. 3A), implying the dependence of astigmatism on defocus for CM200 is much more severe than that for Titan Krios. Furthermore, polar plots were used to show the raw data distribution of the astigmatism used for the line graphs with the same colors. Fig. 3B-D present the polar distribution of astigmatism with varying defocus when the astigmatism is corrected at small (Fig. 3B), medium (Fig. 3C), and large defocus (Fig. 3D) on Titan Krios, corresponding to the red, green, and blue line in Fig. 3A, respectively. It is evident that the astigmatism angle stably points to a certain direction as the astigmatism amplitude gradually increases due to the monotonically ascending (Fig. 3B) or

194 descending defocus (Fig. 3D). In addition, Fig. 3C shows that the astigmatism angle changes  
 195 about 90° when defocus changes bi-directionally after astigmatism minimization. The 90°  
 196 angle change corresponds to the swapping of the major and minor axes of astigmatism.  
 197 Similar distributions can also be seen from the raw data acquired on CM200 (Fig. 3F-H) but  
 198 with larger increase of astigmatism than that on Titan Krios (Fig. 3B-D). Therefore, all the  
 199 analyses above demonstrate the general existence of defocus-dependent astigmatism in the  
 200 objective lens of TEM.

201 For a comprehensive understanding of defocus-dependent astigmatism, we repeated our  
 202 measurement on different days and compared the variation of astigmatism. As shown in Fig.  
 203 4A and E, the slopes of lines are not identical even for the measurements made using the  
 204 same conditions, demonstrating the amount of dependence varies from day to day on both  
 205 Titan Krios (Fig. 4A) and CM200 (Fig. 4E) microscopes. What's more, much more  
 206 pronounced differences in the astigmatism angles were shown in the data collected on Titan  
 207 Krios (Fig. 4B-D) among different days when the astigmatism is initially minimized at a  
 208 small defocus. The differences indicate that the distribution of defocus-dependent astigmatism  
 209 cannot be exactly reproduced even though the defocus is adjusted in the same way. This  
 210 irreproducibility can also be observed from the data collected on CM200 (Fig. 4F-H) when  
 211 the astigmatism correction is performed at a large defocus. Consequently, the comparison of  
 212 the repetitive measurements confirms the variability of defocus-dependent astigmatism in the  
 213 objective lens of TEM.

### 214 **3.4 Magnification-dependent astigmatism**

215 We also used  $s^2stigmator$  to investigate the dependence of astigmatism on magnification and  
 216 to test the implicit assumption of invariant astigmatism at different magnifications for the  
 217 common practice of using a higher magnification for correction of astigmatism than that for  
 218 data acquisition. We first corrected astigmatism at a nominal magnification of 96,000X on  
 219 Titan Krios and 250,000X on CM200 microscope, respectively, then measured the

220 astigmatism as the magnification was stepwise reduced while keeping all other instrument  
 221 parameters unchanged. Fig. 5 shows the change of astigmatism/defocus with magnification  
 222 for Titan Krios and the variability of this change across multiple measurements. At each  
 223 magnification, we collected twenty images, plotted the distribution of astigmatism in polar  
 224 coordinate (Fig. 5A-C), and then calculated their mean and RMSD of astigmatism (blue  
 225 line)/defocus (red line) represented as points and error bars (may be too small to be visible) in  
 226 Fig. 5D-F. When repeating the measurements on Titan Krios, the changes of defocus (red  
 227 lines in Fig. 5D-F) follow a similar pattern, but the profiles of both astigmatism amplitude  
 228 (blue lines in Fig. 5D-F) and astigmatism angle (Fig. 5A-C) are irreproducible. Similar  
 229 results were also found for CM200 (Fig. 6) in which the defocus tends to increase with lower  
 230 magnifications (red lines in Fig. 6D-F), rather than decrease as shown for Titan Krios (red  
 231 lines in Fig. 5D-F). All these data demonstrate the existence of magnification-dependent  
 232 astigmatism and its stochastic fluctuations for both high-end and low-end TEM.

233

234

## 235 4. Discussion

236 In contrast to the dramatic progress in the automated cryo-EM data acquisition and image  
237 processing methods, little has changed for the microscope alignment tasks before data  
238 acquisition. In this paper, inspired by the observations of defocus-astigmatism correlations in  
239 experimental cryo-EM datasets, we have discovered the defocus/magnification-dependence of  
240 objective lens astigmatism and their stochastic variability using our recently published tool  
241 *s<sup>2</sup>stigmator*. These findings have essentially invalidated a basic assumption of current cryo-  
242 EM imaging strategy that assumes constant astigmatism for the significantly different  
243 defocuses/magnifications used in microscope alignment stage and final data acquisition stage.

244 **Vector summation model of the net astigmatism and the single pass tuning strategy.** As  
245 shown here and in our previous work (Yan et al., 2017), *s<sup>2</sup>stigmator* can help achieve accurate  
246 correction of objective lens astigmatism at any imaging condition using a single pass tuning  
247 strategy. Understanding the principle of this single-pass tuning strategy will help further  
248 unveil the underlying theory of astigmatism variations with imaging parameters. Fig. 7  
249 illustrates the vector diagrams (Fig. 7B-D) of three key points in a typical trajectory (Fig. 7A),  
250 including the initial point (⊠ in Fig. 7A), the optimal point (⊙ in Fig. 7A) in the arc-like  
251 segment when tuning the first stigmator (e.g. MY), and the final point at the center (⊙ in Fig.  
252 7A) after tuning the other stigmator (e.g. MX). The corresponding stigmator MX/MY values  
253 are labelled in parentheses next to the circled numbers. In Fig. 7B,  $\vec{V}_{obj}$ ,  $\vec{V}_{MX}^0$ ,  $\vec{V}_{MY}^0$  represents  
254 the initial state of the astigmatism of the objective lens, and the correction field of the  
255 stigmator MX and MY, respectively.  $\vec{V}_{sum}^0$  is the summation of these three vectors and  
256 corresponds to the point ⊠ in Fig. 7A. Here  $\vec{V}_{obj}$  can be considered as a constant vector in a  
257 short period of time, e.g. during astigmatism correction, while the correction field  $\vec{V}_{MX}$  and  
258  $\vec{V}_{MY}$  will be varied to cancel  $\vec{V}_{obj}$  in order to minimize astigmatism. However, the orientations

259 of  $\vec{V}_{MX}^0$  and  $\vec{V}_{MY}^0$  are fixed and the angle between them is also fixed at  $45^\circ$ , which are  
260 determined by the design of the octupole objective lens stigmator (Hawkes, 2013; Rai-  
261 Choudhury, 1997) assembly containing two interdigitated quadruple stigmators with  $45^\circ$   
262 offset. When the stigmators are adjusted, the  $\vec{V}_{MX}$  and  $\vec{V}_{MY}$  vectors will change lengths  
263 without turning. The astigmatism correction task is to find the optimal lengths for both  
264 stigmator vectors so that the sum of the two correction vectors will be exactly inverse of the  
265 objective astigmatism vector  $\vec{V}_{obj}$  (i.e. same length but opposite direction). In Fig. 7C, only  
266 the stigmator MY is adjusted (red line in Fig. 7C) until it reaches the optimal length ( $\vec{V}_{MY}^1$ ) at  
267 which its vector sum with  $\vec{V}_{obj}$  ( $\vec{V}_{sum}^1$ ) is along the direction of  $\vec{V}_{MX}^1$ . In this process, the  
268 resulted points (i.e. the net astigmatism, or the sum of the three vectors) of the trajectory  
269 shown in Fig. 7A exhibit an arc-like segment. Here the stigmator MX does not change  
270 ( $\vec{V}_{MX}^1 = \vec{V}_{MX}^0$ ) and  $\vec{V}_{sum}^1$  is along the direction of  $\vec{V}_{MX}^1$ , corresponding to the point ① in Fig. 7A.

271 In Fig. 7D, only the stigmator MX is adjusted to cause its correction field vector  $\vec{V}_{MX}$  to  
272 change length (green line in Fig. 7D) until the overall summation of vectors is 0 ( $\vec{V}_{sum}^2 = 0$ ,  
273 ② in Fig. 7A). In this part of trajectory, the resulted points should directly move to the origin,  
274 forming a straight trace segment. As demonstrated in Fig. 7, the orientation of the straight  
275 trace segment is determined by the manufacturer's setting of the stigmator MX's direction.  
276 This finding can explain why the orientations of trajectories shown in Fig. S1 are the same,  
277 independent of defocus and magnification, when the two stigmators are adjusted in the order  
278 of MY first then MX. On the contrary, if the order of stigmators is switched during  
279 adjustment (MX first, then MY), the trajectory will rotate  $45^\circ$  and the straight trace segment  
280 will represent the direction of stigmator MY (Fig. 2A). This vector summation model is also  
281 validated on CM200 when the rotation of trajectories between different magnifications due to  
282 the imperfect rotation-free function is considered. The analysis described above explains the  
283 relationship of the objective lens astigmatism and the correction fields generated by the  
284 stigmators, and how the stigmators can be controlled to optimally compensate the objective

285 lens astigmatism. The vector summation model described here further refines our previous  
286 model (Yan et al., 2017).

287 **Defocus-dependent astigmatism.** During single particle cryo-EM image acquisition, the  
288 defocuses for different images are intentionally varied to average out the effect of zero-nodes  
289 of CTF and obtain signals at all frequencies (Cheng et al., 2015; Penczek, 2010; Zhu et al.,  
290 1997). Nevertheless, the discovery of defocus-dependent astigmatism (Fig. 3) implies a  
291 significant problem of re-emerging astigmatism in this imaging strategy. Fig. 8 uses vector  
292 diagrams to explain the case of corrected astigmatism (Fig. 8A), and the re-emerged  
293 astigmatism after increasing (Fig. 8B) and decreasing (Fig. 8C) defocus. As can be seen  
294 from Fig. 8A, the total summation vector  $\vec{V}_{sum} = 0$  when  $\vec{V}_{obj}$  is canceled by  $\vec{V}_{stigmator}$ .  
295 Here  $\vec{V}_{obj}$  and  $\vec{V}_{stigmator}$  represent the astigmatism of objective lens and the combined  
296 correction field of the two stigmators, respectively. Moreover, the objective lens astigmatism  
297 ( $\vec{V}_{obj}$ ) is assumed to be proportional to the strength of objective lens current ( $I_{obj}$ ) as

$$298 \quad \vec{V}_{obj} = k I_{obj} \cdot \vec{e} \quad (1)$$

299 where  $\vec{e}$  is a unit vector representing the direction of the objective lens astigmatism ( $\vec{V}_{obj}$ ) and  
300  $k$  is a scaling factor representing how strong the dependence is between  $\vec{V}_{obj}$  and  $I_{obj}$ . In Fig.  
301 8A, the astigmatism is corrected completely and the shape of Thon rings is perfectly circular  
302 (Fig. 8D). However, to increase defocus the objective lens current needs to be reduced to  
303 weaken the lens bending power, leading to a smaller objective lens astigmatism (blue arrow,  
304  $\vec{V}_{dft}$ ). The correction fields by the two stigmator ( $\vec{V}_{stigmator}$ ), which have not been changed  
305 from previous values optimized for a larger amount of objective lens astigmatism, now over-  
306 corrects the new, reduced objective lens astigmatism. A non-zero  $\vec{V}_{sum}$  (Fig. 8B) now appears  
307 and the Thon rings (Fig. 8E) become elongated. The analysis in Fig. 8B agrees with the  
308 observations from the Titan Krios (red line in Fig. 3A, Fig. 3B) and CM200 (red line in Fig.  
309 3E, Fig. 3F) microscopes in the case of increasing defocus. Similarly, another non-zero  $\vec{V}_{sum}$

(Fig. 8C) appears in the opposite direction when defocus decreases, resulting in the Thon rings (Fig. 8F) becoming elongated along the perpendicular direction (blue arrow,  $\vec{V}_{df\perp}$ ), since the switch of  $\vec{V}_{sum}$  direction is equivalent to change the ellipticity by  $90^\circ$ . The analysis in Fig. 8C also agrees with the observed defocus-dependence of astigmatism as defocus decreases (blue line in Fig. 3A, Fig. 3D for Titan Krios; blue line in Fig. 3E, Fig. 3H for CM200). Combining the vector diagrams in both Fig. 8B and C, the bi-directional increment of astigmatism can also be clearly understood, as well as the  $90^\circ$  angle between two branches in the polar plots (green line in Fig. 3A, Fig. 3C for Titan Krios; green line in Fig. 3E, Fig. 3G for CM200) when the astigmatism is minimized at the middle point of the defocus range. This finding of defocus-dependent astigmatism is also consistent with theoretic predictions based on Zernike polynomial expression of lens aberrations (Vargas et al., 2013).

**Quantification of objective lens asymmetry.** In the line plots from the Titan Krios (Fig. 3A) and CM200 (Fig. 3E), it is evident that the slopes of the linear trends are different for the two instruments. The slope measures how strong the dependence of astigmatism on defocus is and should be proportional to the scaling factor  $k$  in Eq. (1). For a perfectly round lens  $k$  is equal to 0 and as asymmetry in the lens increases, the larger  $k$  becomes. Therefore, we can use  $k$  as a parameter to quantify the quality of a TEM magnetic lens in terms of its cylindrical symmetry. A lens with smaller  $k$  will be a higher quality lens. Using this criterion, the objective lens of the Titan Krios microscope is more cylindric than that of CM200 microscope. This is consistent with the common understanding of current generation Titan Krios as a higher quality TEM than the CM200 microscope which was produced more than two decades ago. We propose that the defocus-dependent plots of astigmatism as shown in Fig. 3A and 3E are convenient measurements of the asymmetry level of the objective lens of a TEM instrument. Such quantitative measurements can be useful in several applications. For example, it can be used as one of the acceptance tests after the installation of a new TEM instrument. It can also be used to monitor the performance of the objective lens and to detect potential deterioration, for example, caused by a large contamination in the objective lens area.

337 **Stochastic variations of defocus-dependent astigmatism.** The defocus-dependent  
 338 astigmatism, including both the slope and the direction, was found to vary in our data (Fig. 4)  
 339 when the same measurement was repeated after more than two-weeks. While the astigmatism  
 340 of objective lens ( $\vec{V}_{obj}$ ) is considered stable within a short period time (a few hours to one or  
 341 two days), it is also well-known that astigmatism tends to vary. As a result, it is a common  
 342 practice to check and re-correct astigmatism as one of the daily-instrument alignment tasks.  
 343 Our measurements (Fig. 4) have thus quantitatively verified the variability and validated the  
 344 need for daily correction of astigmatism. Such variability can also be explained using the  
 345 vector summation model (Fig. 9).  $\vec{V}_{obj}$  can vary due to the change of either the unit vector  $\vec{e}$   
 346 direction or the amplitude of the scaling factor  $k$  (Eq. (1)) at different times. In the vector  
 347 diagram (Fig. 9), the varying  $\vec{V}_{obj}$  (the objective lens astigmatism, blue arrows) is  
 348 compensated by corresponding  $\vec{V}_{stigmator}$  (stigmator values, red arrows) that needs to be  
 349 updated from day to day. There is a wide variety of reasons for the stochastic changes of  $\vec{e}$   
 350 and  $k$ , such as objective lens asymmetry due to imperfect manufacturing processes, electronic  
 351 instability of the voltage and power supplies, column contaminations, temperature  
 352 fluctuations of the objective lens chilling water, *etc.* (Barthel and Thust, 2013).

353 **Magnification-dependent astigmatism.** In addition to the defocus-dependent astigmatism,  
 354 magnification-dependent astigmatism was also observed (Figs. 5 and 6). This implies that  
 355 noticeable astigmatism would re-emerge during data collection if a different magnification is  
 356 used for the correction of astigmatism during instrument alignment. Compared with the  
 357 variability of astigmatism due to defocus, the astigmatism dependence on magnification is  
 358 even more variable. When the same test was repeated three times on Titan Krios on the same  
 359 day, the distribution of astigmatism at different magnifications is considerably different in  
 360 both amplitude and angle (Fig. 5A-C). In the line plot for each measurement, the profile of  
 361 astigmatism variation appears random in different tests (blue lines in Fig. 5D-F) while the  
 362 profile of defocus variation is much more reproducible. Similar observations were obtained



363 for both Titan Krios (Fig. 5) and CM200 (Fig. 6), which indicates that the defocus change is  
364 stable but the astigmatism change is unpredictable.

365 Modern TEM instruments usually use multiple imaging lenses, including an objective lens, a  
366 diffraction lens, an intermediate lens, and two projector lenses, to provide a wide range of  
367 magnifications. The astigmatism measured in the TEM image is a combined result of the  
368 astigmatism of all these lenses. The two stigmators actually correct the combined astigmatism  
369 of all these imaging lenses. When the magnification is changed, the current of all or a subset  
370 of these lenses would change, which leads to the change of individual lens astigmatism (Eq.  
371 (1)) and the combined astigmatism. As the stigmators have been tuned to correct the  
372 combined astigmatism at a particular magnification, the change of magnification will thus  
373 lead to re-emerging of astigmatism in the image at a different magnification. Since the  
374 currents of these lenses need to be changed in a non-linear pattern to achieve rotation-free  
375 imaging at multiple total magnifications, the combined astigmatism thus also varies in a non-  
376 linear pattern (Figs. 5 and 6). The irreproducibility of the profile of magnification-dependent  
377 astigmatism are caused by some random factors, such as column contaminations. Since the  
378 change of any one of the five lenses will change the combined astigmatism, it is thus not  
379 surprising the irreproducibility of the profile of magnification-dependent astigmatism is  
380 significantly worse than the irreproducibility of the profile of defocus-dependent astigmatism  
381 that is only affected by a single lens, the objective lens. In contrast, the profile of  
382 magnification-dependent defocus is more reproducible than that of magnification-dependent  
383 astigmatism as the pattern of current change is the same and the focus length of the lenses is  
384 more resistant to the random factors affecting the lens astigmatism.

385 **Recommendations for optimal TEM operations.** The astigmatism of TEM images has been  
386 shown here to vary with changes in imaging conditions (e.g. defocus, magnification),  
387 indicating that correction of astigmatism at high magnification and near-focus conditions by  
388 the current approach will not be optimal after switching to different conditions for data  
389 acquisition. What's worse, the dependence of astigmatism on the imaging conditions varies

390 from time to time, so that astigmatism cannot be reliably compensated by pre-calibration of  
 391 the instrument. Based on our systematic measurements and analyses in this work, we suggest  
 392 that 1) the magnification used for instrument alignment should be the same as the one used  
 393 for data collection; 2) the defocus used for correction of astigmatism during instrument  
 394 alignment should be set at the median defocus of the defocus range intended for subsequent  
 395 data collection; 3) the magnification used for the focus-mode in the search-focus-exposure  
 396 iterations of low-dose imaging should be the same magnification that is used for the exposure  
 397 mode. To optimally correct the astigmatism for all images, a fast, accurate, and automated  
 398 method needs to be developed to avoid the defocus-dependent astigmatism by adaptively  
 399 correcting the astigmatism at all focuses.

400

401

402    **Acknowledgements**

403    This work was supported in part by NIH grant (1R01AI111095). We thank the Purdue Cryo-  
404    EM Facility (<http://cryoem.bio.purdue.edu>) for the use of the Titan Krios and CM200  
405    microscopes. We thank Dr. Dinesh Yernool, Dr. Anoop Narayanan, and Mr. Frank Vago for  
406    the RNA polymerase dataset, and Ms. Brenda Gonzalez for her assistance in preparation of  
407    the manuscript.

408

409

410

411

## 412 **Figure Legends**

413 **Fig. 1 Observations of the relationship between defocus and astigmatism in**  
 414 **experimental cryo-EM datasets.** The EMPIAR ID (Iudin et al., 2016), instrument, and  
 415 magnification are marked at the lower right corner of each plot.

416 **Fig. 2 Performance of  $s^2$ stigmator method and the single-pass tuning strategy.** (A) A  
 417 screenshot of the trajectory from Titan Krios microscope obtained at 1000 nm defocus, a  
 418 nominal magnification of 22,500X and 25 e/Å<sup>2</sup> dose with images recorded on a Gatan K2  
 419 Summit direct electron detector operated at counted mode using 15 e/pixel/second dose rate  
 420 and 3s exposure time. Stigmator MX was adjusted first (arc-like segment) and then MY was  
 421 adjusted (straight segment). (B) A screenshot of trajectory from CM200 microscope obtained  
 422 at 1000 nm defocus, a nominal magnification of 66,000X and 40 e/Å<sup>2</sup> dose with images  
 423 recorded on a Gatan UltraScan 4k CCD with 3s exposure time. Stigmator MY was adjusted  
 424 first (arc-like segment) and then MX was adjusted (straight segment). The wide blue arrow  
 425 indicates the optimal point with minimum astigmatism in the arc-like segment of each  
 426 trajectory.

427 **Fig. 3 Defocus-dependent astigmatism.** (A) The increment of astigmatism with the change  
 428 of defocus on Titan Krios microscope when the astigmatism is corrected at small (red),  
 429 medium (green) and large (blue) defocus, respectively. (B-D) The polar distribution of all  
 430 data obtained from Titan Krios microscope when the astigmatism is corrected at small (B),  
 431 medium (C) and large (D) defocus, corresponding to the line with the same color in (A),  
 432 respectively. (E) The increment of astigmatism with the change of defocus on CM200  
 433 microscope obtained from the same experiment described in (A). The correlation between (E)  
 434 and (F-H) is the same as that between (A) and (B-D). In the line plots (A, E), the point and  
 435 error bar at each defocus represent the mean and RMSD of astigmatism from ten images,  
 436 respectively.

**Fig. 4 Variability of defocus-dependent astigmatism.** (A) The profile of astigmatism increment as defocus increases on Titan Krios microscope when the astigmatism is minimized at small defocus on three different days. (B-D) The polar distribution of all data from the repeated experiments on Titan Krios microscope described in (A). Each polar distribution corresponds to the line with the same color as in (A). (E) The profile of astigmatism increment as defocus decreases on CM200 microscope when the astigmatism is minimized at large defocus on three different days. The correlation between (E) and (F-H) is the same as that between (A) and (B-D). In the line plots (A, E), the point and error bar at each defocus represents the mean and RMSD of astigmatism from ten images, respectively.

**Fig. 5 Magnification-dependent astigmatism detected on Titan Krios microscope.** (A-C) Plots of astigmatism polar distribution with stepwise reduction of magnifications in three repeated measurements in a single day when the astigmatism is corrected at a nominal magnification of 96,000X. (D-F) The profiles of the variations of astigmatism (blue line) or defocus (red line) with the change of magnifications, corresponding to the measurements in (A-C). At each magnification, twenty images were collected and their astigmatism and defoci were calculated. The point and error bar represent the mean and RMSD of astigmatism in the blue line or defocus in the red line, respectively. The error bar may be too small to be visible in the line plot.

**Fig. 6 Magnification-dependent astigmatism detected on CM200 microscope.** The measurements are the same as described in Fig. 5. The only difference being that the astigmatism is corrected at a nominal magnification of 250,000X on the CM200.

**Fig. 7 Vector diagrams to illustrate the principle of single-pass tuning strategy for astigmatism correction.** (A) A screenshot of the trajectory on the Titan Krios microscope in which three key points are marked by red circled numbers ①, ②, ③, corresponding to the vector diagrams in (B-D), respectively. The corresponding stigmator MX/MY values are labelled in parentheses next to the circled numbers. (B) Initial point ①. The astigmatism of the objective lens, the correction fields of stigmator MX and MY are represented by

464  $\vec{V}_{obj}$ ,  $\vec{V}_{MX}^0$ ,  $\vec{V}_{MY}^0$ , and their summation is represented by  $\vec{V}_{sum}^0$ . It is noted that  $\vec{V}_{obj}$  is assumed as  
 465 a constant vector here, the directions of  $\vec{V}_{MX}^0$  and  $\vec{V}_{MY}^0$  are fixed and the angle between them is  
 466  $45^\circ$ . (C) The optimal point ① in the arc-like segment. The stigmator MY first reaches its  
 467 optimal value ( $\vec{V}_{MY}^1$ ) after adjusting along its own direction (red line) until  $\vec{V}_{sum}^1$  is located in  
 468 the direction of the stigmator MX ( $\vec{V}_{MX}^1$ ). Here  $\vec{V}_{sum}^1$  corresponds to the point ① in (A). (D)  
 469 The final point ② of astigmatism correction. The stigmator MX is now adjusted along the  
 470 direction of green line until  $\vec{V}_{sum}^2$  is zero, corresponding to the point ② in (A). Consequently,  
 471 the orientation of the straight trace segment in the trajectory (A) is determined by the  
 472 orientation of stigmator MX.

473 **Fig. 8 Vector diagram to interpret the defocus-dependent astigmatism shown in Fig. 3.**

474 (A-C) Vector diagrams illuminate the state of astigmatism fully corrected at a defocus (A),  
 475 increased defocus after correction (B), decreased defocus after correction (C). Here the red  
 476 arrows represent the combined correction field of the two stigmators ( $\vec{V}_{stigmator}$ ) and the blue  
 477 arrows represent the astigmatism of the objective lens ( $\vec{V}_{obj}$ ) which is proportional to the  
 478 strength of objective lens current. When defocus increases or decreases, the associated  
 479 objective lens astigmatism,  $\vec{V}_{df\uparrow}$  and  $\vec{V}_{df\downarrow}$ , becomes smaller or larger than the original  $\vec{V}_{obj}$   
 480 which is compensated by  $\vec{V}_{stigmator}$ . (D-F) The representative sketches of the shape of Thon  
 481 rings in the astigmatism states corresponding to the vector diagrams depicted in (A-C),  
 482 respectively.

483 **Fig. 9 Vector diagram to interpret the variability of defocus-dependent astigmatism**

484 **shown in Fig. 4.** Here the vector representing the astigmatism of the objective lens ( $\vec{V}_{obj}$ ,  
 485 blue arrows) varies from day to day. The randomness of  $\vec{V}_{obj}$  is determined by the orientation  
 486 of the unit vector in black,  $\vec{e}_1$ ,  $\vec{e}_2$  and  $\vec{e}_3$ , coupled with different scaling factors  $k$  (Eq. (1)).

487 The combined effect of two stigmators ( $\vec{V}_{stigmator}$ ), represented by red arrows, needs to be  
 488 varied accordingly to cancel  $\vec{V}_{obj}$  on different days.

489 **Fig. S1 Representative trajectories of astigmatism correction at varying defocuses and**  
 490 **magnifications on Titan Krios microscope.** (A-C) The screenshots of the trajectories  
 491 acquired at a nominal magnification of 22,500X and defocus 500 nm (A), 1500 nm (B) and  
 492 2500 nm (C), respectively. (D-F) The screenshots of the trajectories acquired at a nominal  
 493 magnification of 22,500X (D), 37,000X (E) and 59,000X (F), respectively, and defocus 2500  
 494 nm.

495 **Fig. S2 Representative trajectories of astigmatism correction at varying defocuses and**  
 496 **magnifications on CM200 microscope.** (A-C) The screenshots of the trajectories acquired at  
 497 a nominal magnification of 66,000X and defocus 1000 nm (A), 2000 nm (B) and 3000 nm (C),  
 498 respectively. (D-F) The screenshots of the trajectories acquired at a nominal magnification of  
 499 200,000X (D), 250,000X (E) and 310,000X (F), respectively, and defocus 2000 nm. The  
 500 angles of the straight trace segments are 65°, 51° and 25°, respectively. And the difference  
 501 between two adjacent trajectories are 14° and 26°. (G-I) The real space images collected at a  
 502 nominal magnification of 200,000X (G), 250,000X (H) and 310,000X (I), respectively. The  
 503 rotation of the red dash line represents the rotation of the image in real space with the change  
 504 of magnifications. The angles of the red dash lines are 115°, 101° and 75°, respectively. And  
 505 the angular difference between two adjacent images are 14° and 26°, in agreement with those  
 506 of the trajectories shown in (D-F).

507

508

509

## 510     **References**

- 511     Barthel, J., Thust, A., 2013. On the optical stability of high-resolution transmission electron  
512             microscopes. *Ultramicroscopy* 134, 6–17.
- 513     Cheng, Y., Grigorieff, N., Penczek, P.A., Walz, T., 2015. A primer to single-particle cryo-  
514             electron microscopy. *Cell* 161, 438–449.
- 515     Grant, T., Grigorieff, N., 2015. Automatic estimation and correction of anisotropic  
516             magnification distortion in electron microscopes. *J. Struct. Biol.* 192, 204–208.
- 517     Grassucci, R.A., Taylor, D., Frank, J., 2008. Visualization of macromolecular complexes  
518             using cryo-electron microscopy with FEI Tecnai transmission electron microscopes. *Nat.*  
519             *Protoc.* 3, 330–339.
- 520     Hawkes, P.W., 2013. *The Beginnings of Electron Microscopy*. Academic Press.
- 521     Ishizuka, K., 1994. Coma-free alignment of a high-resolution electron microscope with three-  
522             fold astigmatism. *Ultramicroscopy* 55, 407–418.
- 523     Iudin, A., Korir, P.K., Salavert-Torres, J., Kleywegt, G.J., Patwardhan, A., 2016. EMPIAR: a  
524             public archive for raw electron microscopy image data. *Nat. Methods* 13, 387–388.
- 525     Mindell, J.A., Grigorieff, N., 2003. Accurate determination of local defocus and specimen tilt  
526             in electron microscopy. *J. Struct. Biol.* 142, 334–347.
- 527     Penczek, P.A., 2010. Image restoration in cryo-electron microscopy. *Methods Enzymol.* 482,  
528             35–72.
- 529     Rai-Choudhury, P., 1997. *Handbook of Microlithography, Micromachining, and*  
530             *Microfabrication: Microlithography*. SPIE Press.
- 531     Sun, J., Li, H., 2010. How to operate a cryo-electron microscope. *Methods Enzymol.* 481,  
532             231–249.
- 533     Thon, F., 1971. Phase Contrast Electron Microscopy, in: *Electron Microscopy in Material*  
534             *Science*. pp. 571–625.
- 535     Vargas, J., Otón, J., Marabini, R., Jonic, S., de la Rosa-Trevín, J.M., Carazo, J.M., Sorzano,  
536             C.O.S., 2013. FASTDEF: fast defocus and astigmatism estimation for high-throughput



537 transmission electron microscopy. *J. Struct. Biol.* 181, 136–148.

538 Yan, R., Li, K., Jiang, W., 2017. Real-time detection and single-pass minimization of TEM  
539 objective lens astigmatism. *J. Struct. Biol.* 197, 210–219.

540 Yu, G., Li, K., Liu, Y., Chen, Z., Wang, Z., Yan, R., Klose, T., Tang, L., Jiang, W., 2016. An  
541 algorithm for estimation and correction of anisotropic magnification distortion of cryo-  
542 EM images without need of pre-calibration. *J. Struct. Biol.* 195, 207–215.

543 Zemlin, F., Weiss, K., Schiske, P., Kunath, W., Herrmann, K.-H., 1978. Coma-free alignment  
544 of high resolution electron microscopes with the aid of optical diffractograms.  
545 *Ultramicroscopy* 3, 49–60.

546 Zhu, J., Penczek, P.A., Schröder, R., Frank, J., 1997. Three-dimensional reconstruction with  
547 contrast transfer function correction from energy-filtered cryoelectron micrographs:  
548 procedure and application to the 70S Escherichia coli ribosome. *J. Struct. Biol.* 118,  
549 197–219.

Fig. 1

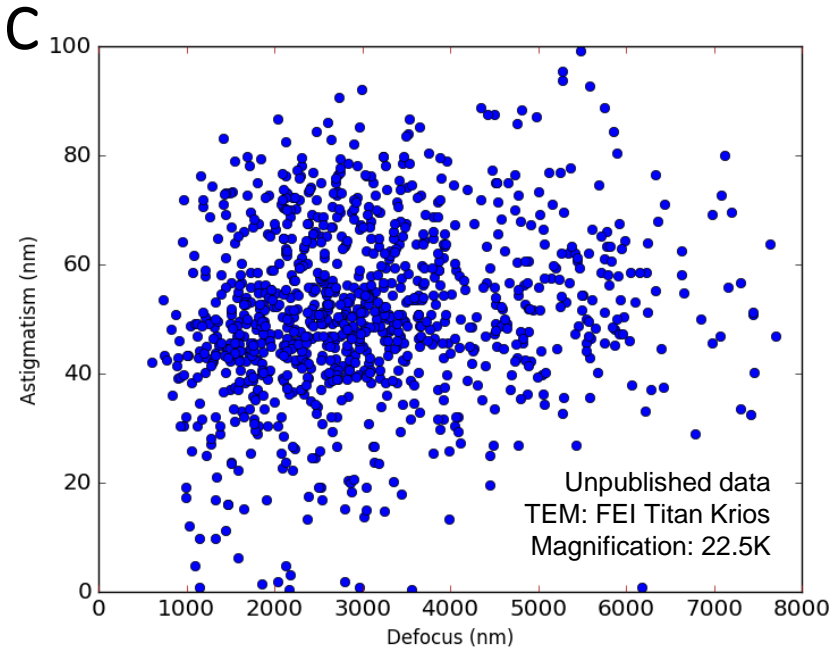
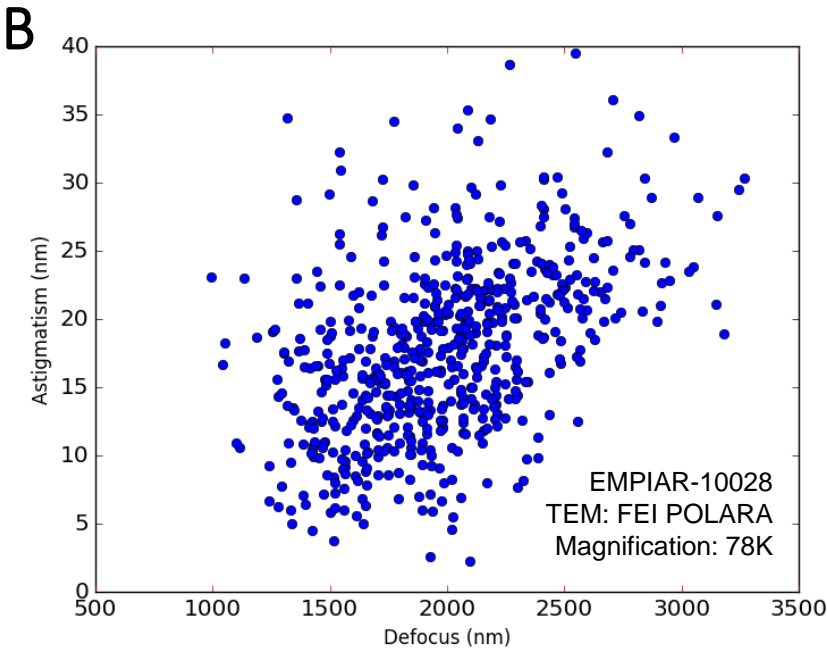
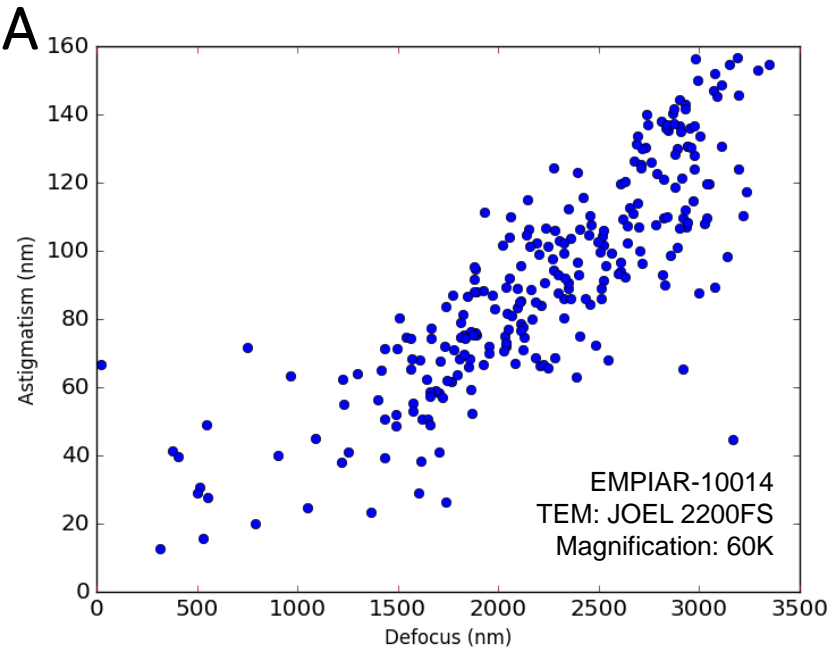


Fig. 2

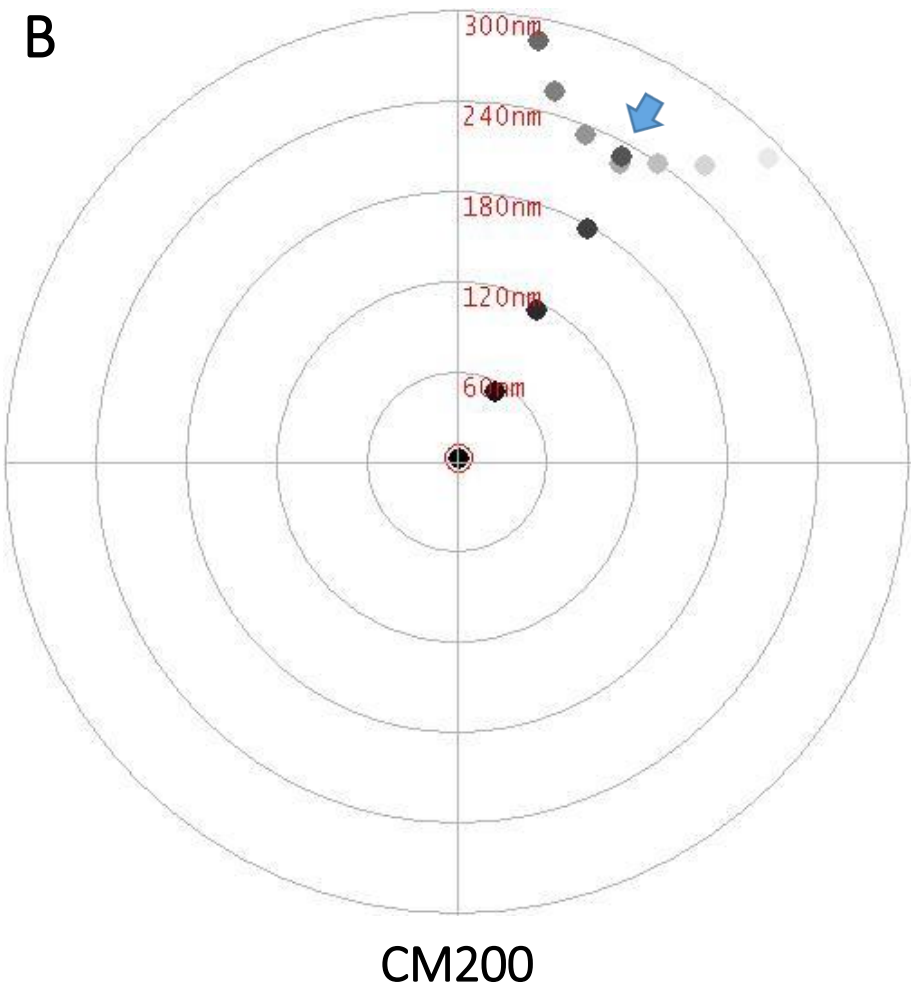
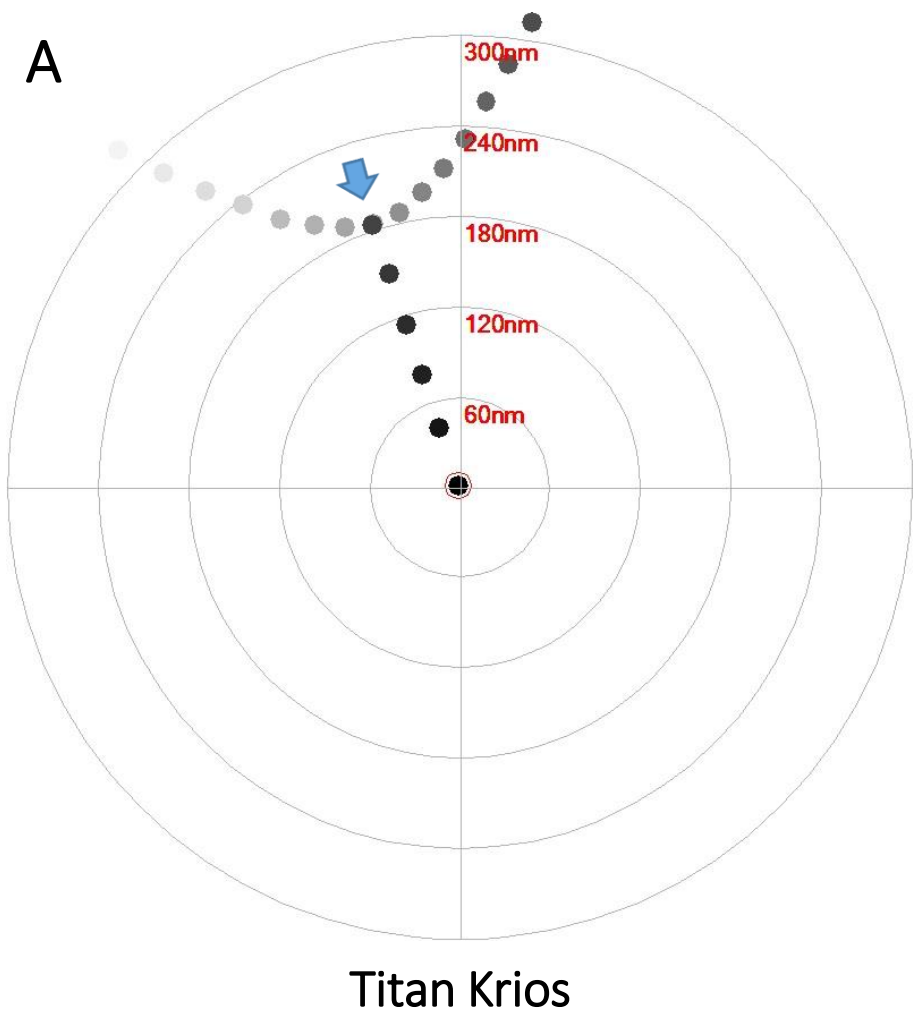


Fig. 3

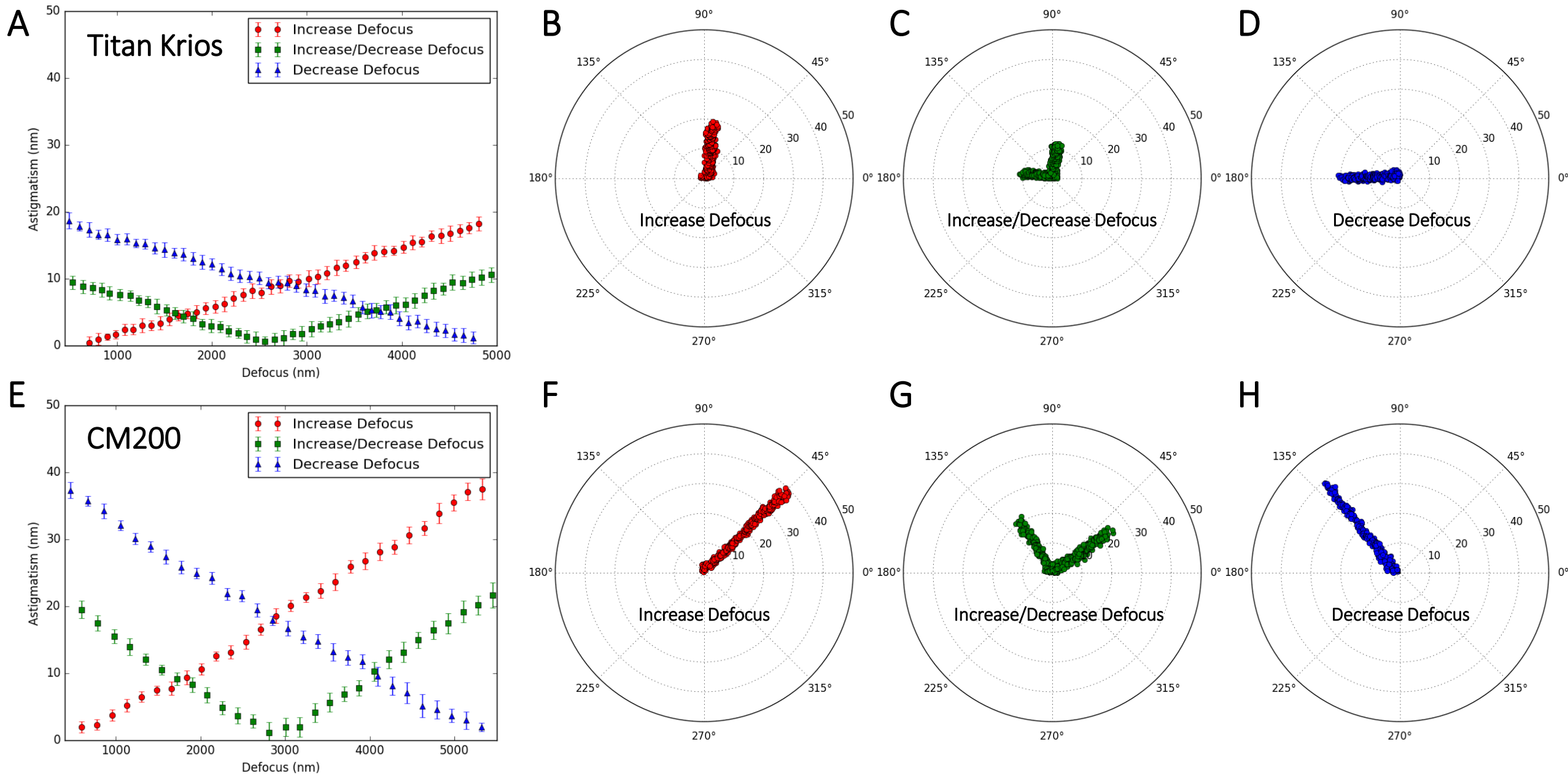


Fig. 4

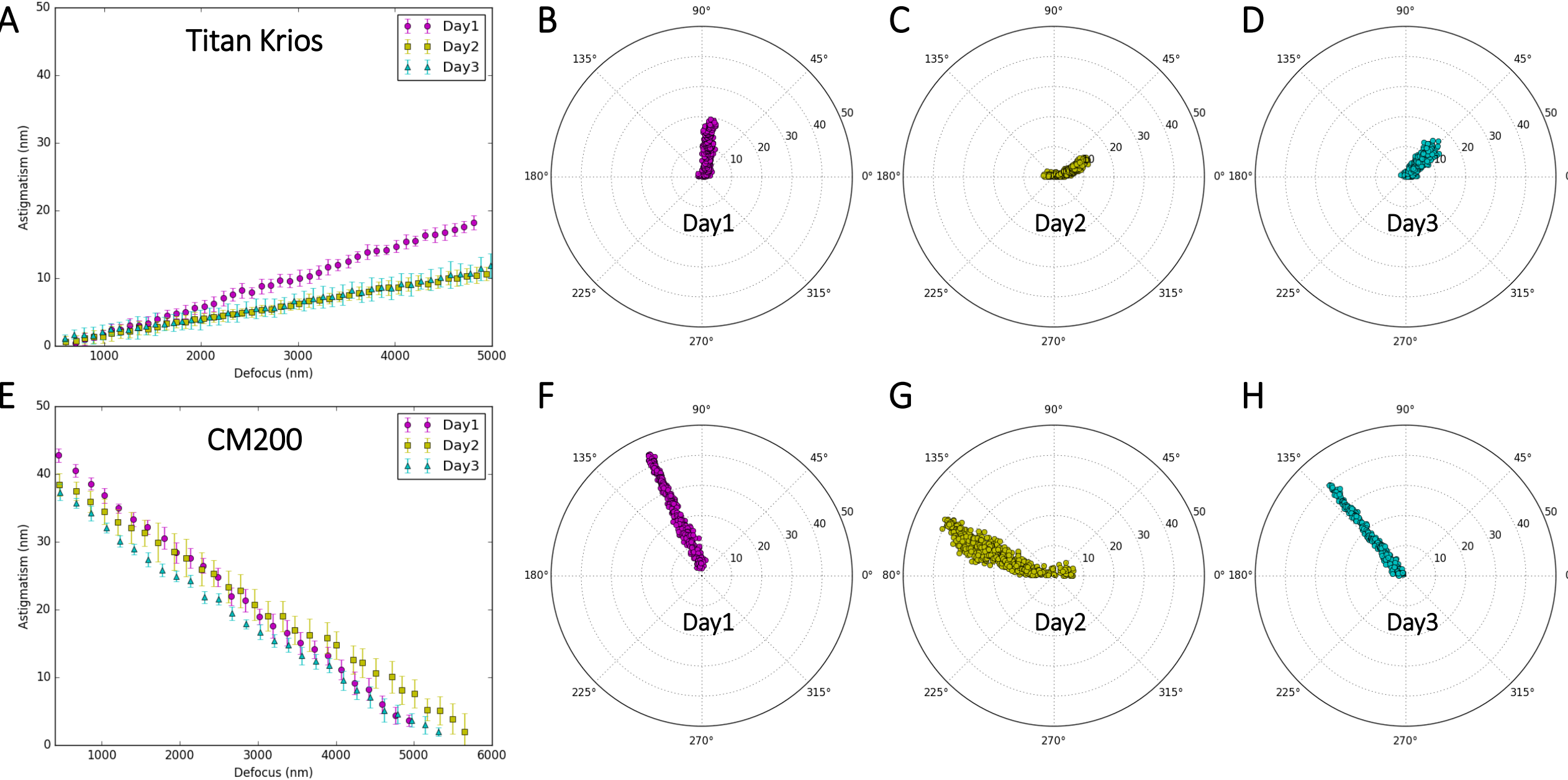


Fig. 5

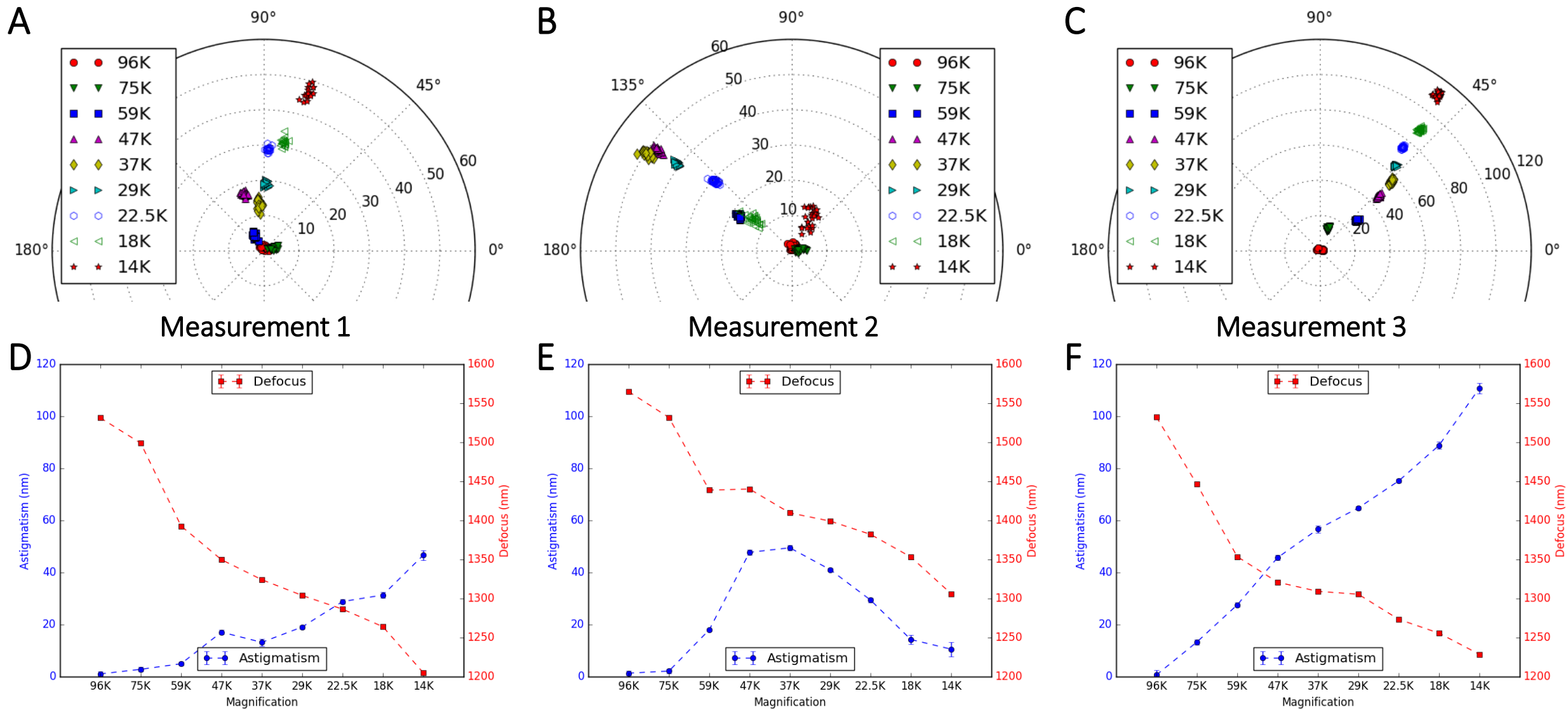


Fig. 6

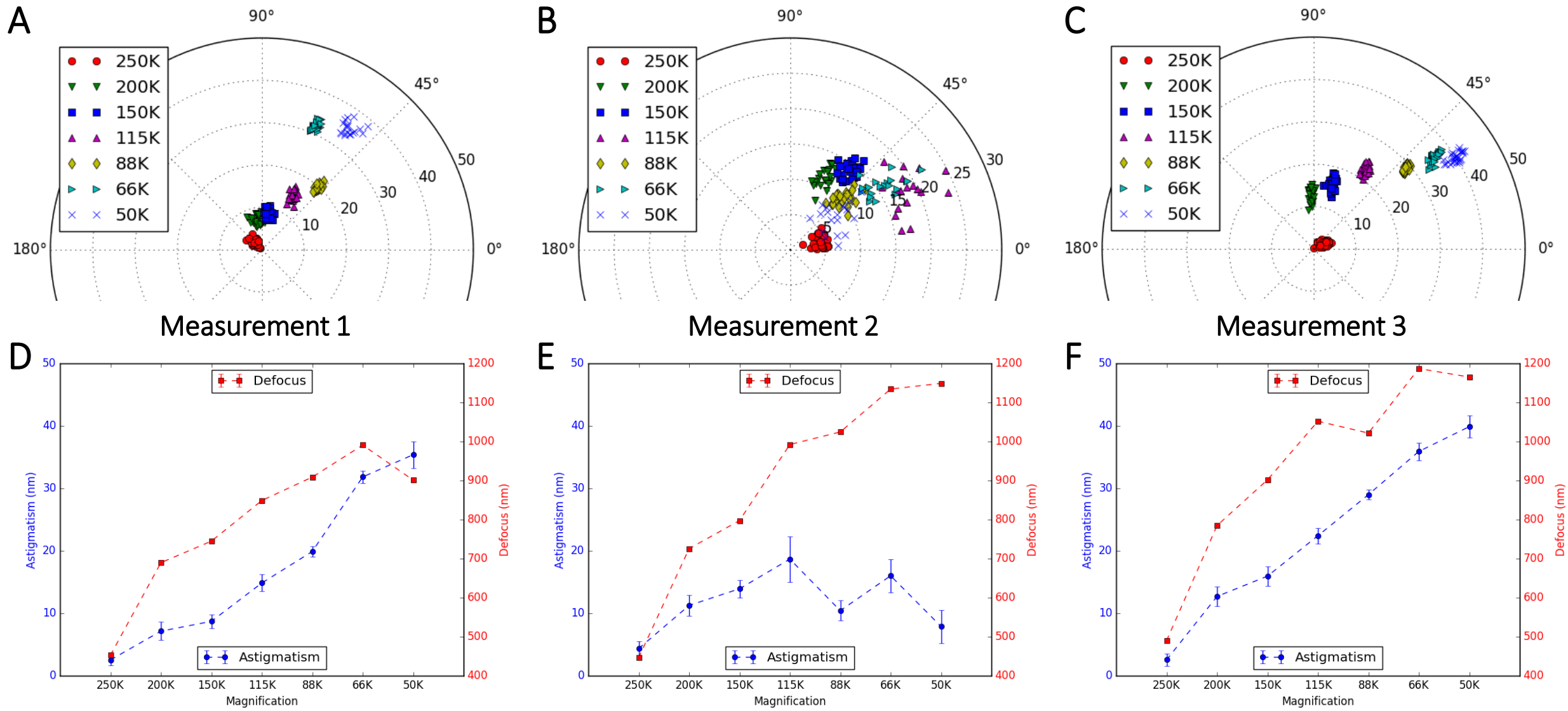


Fig. 7

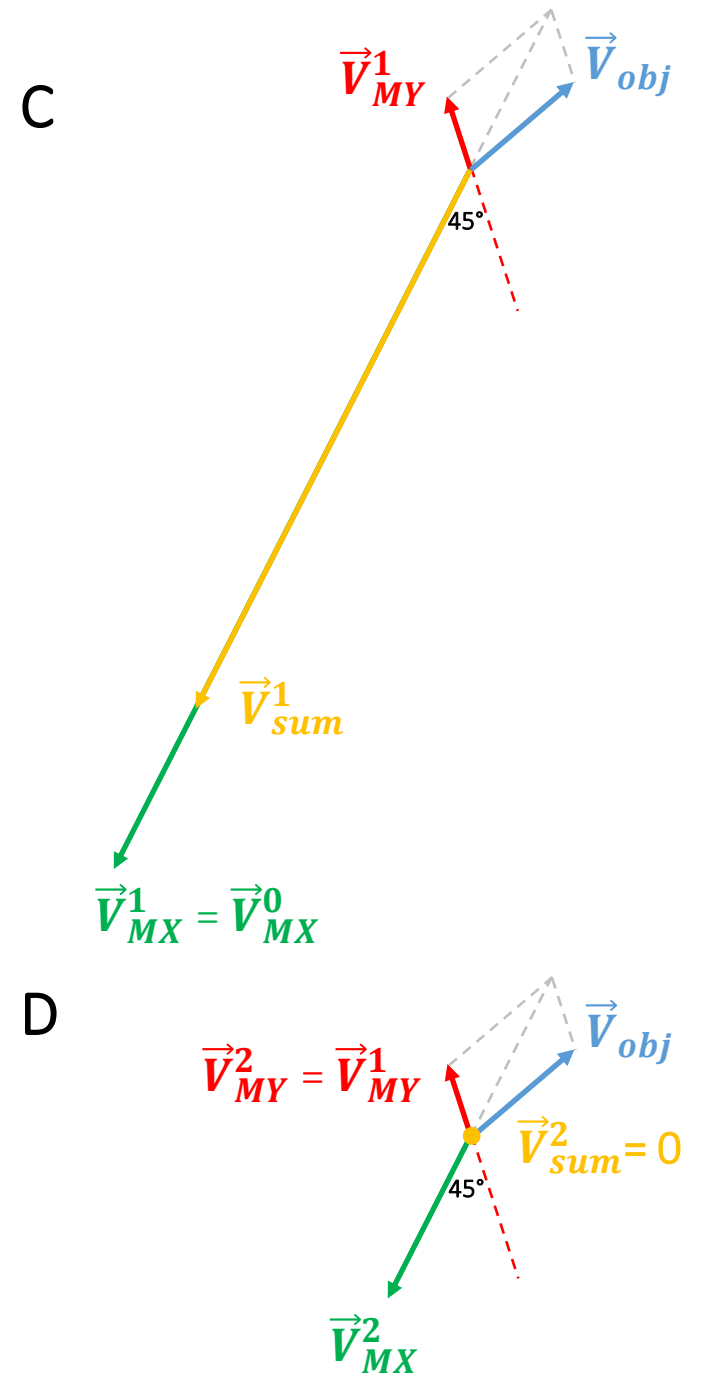
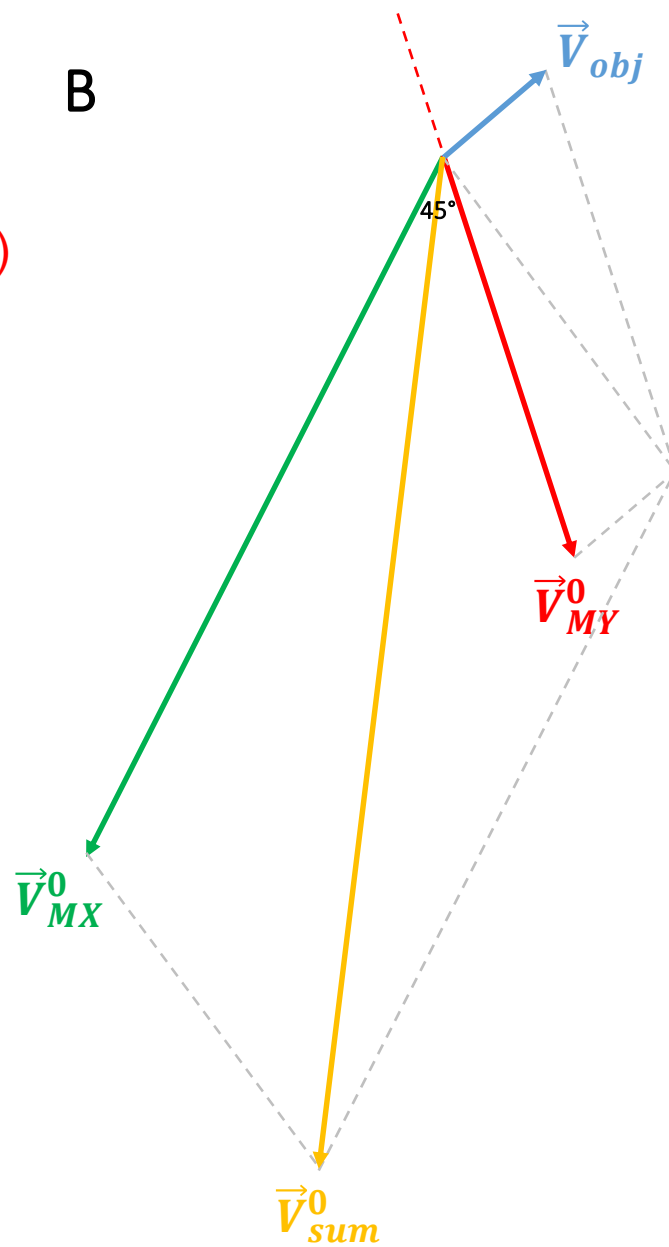
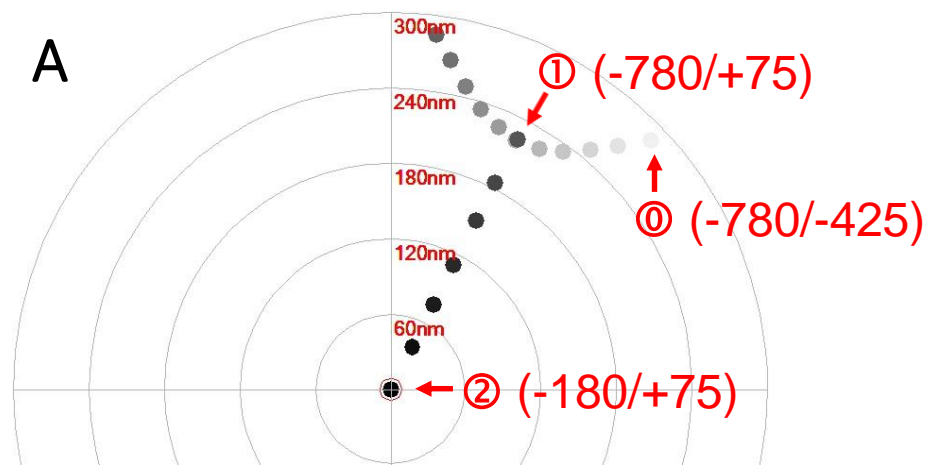




Fig. 8

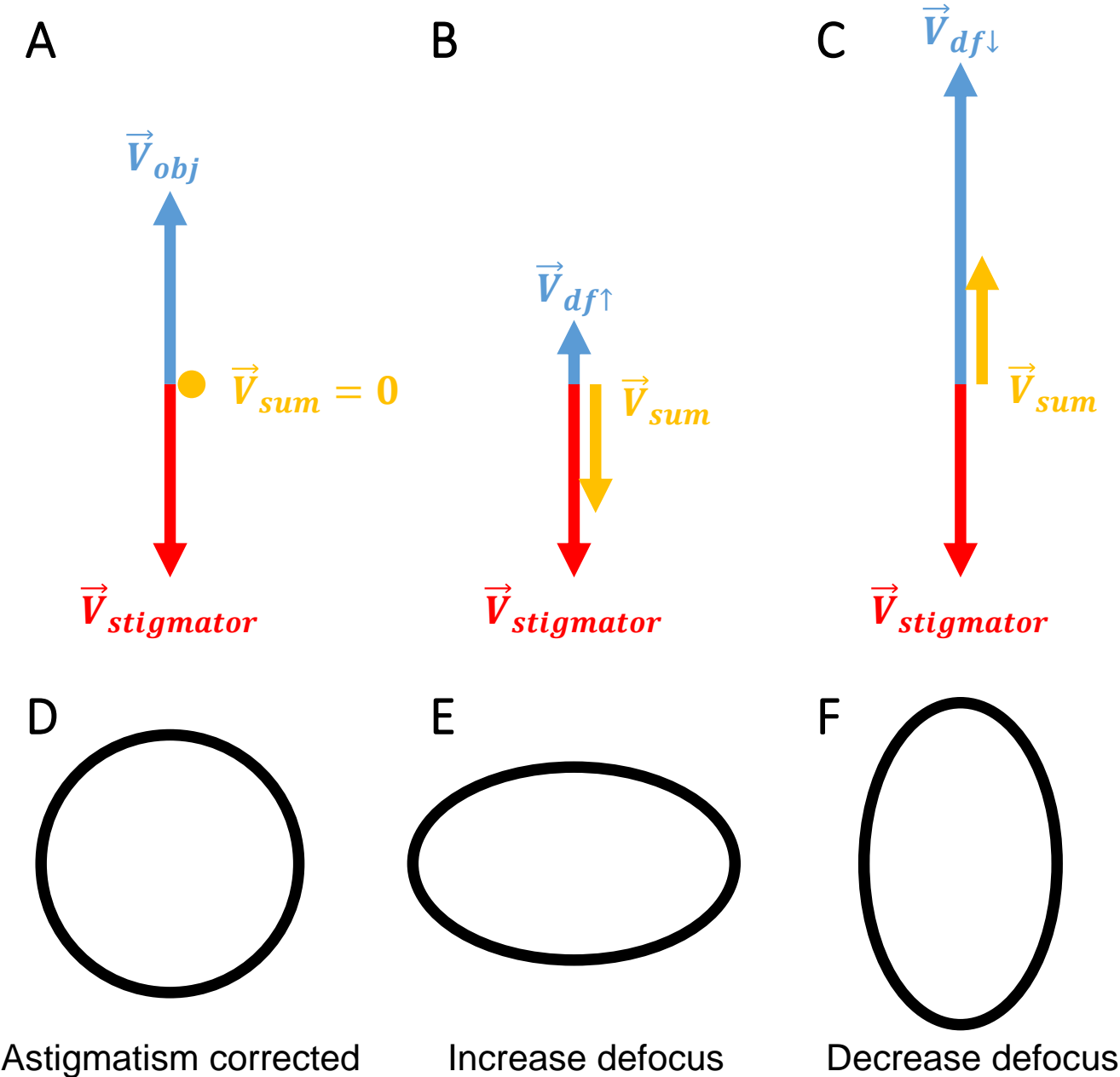


Fig. 9

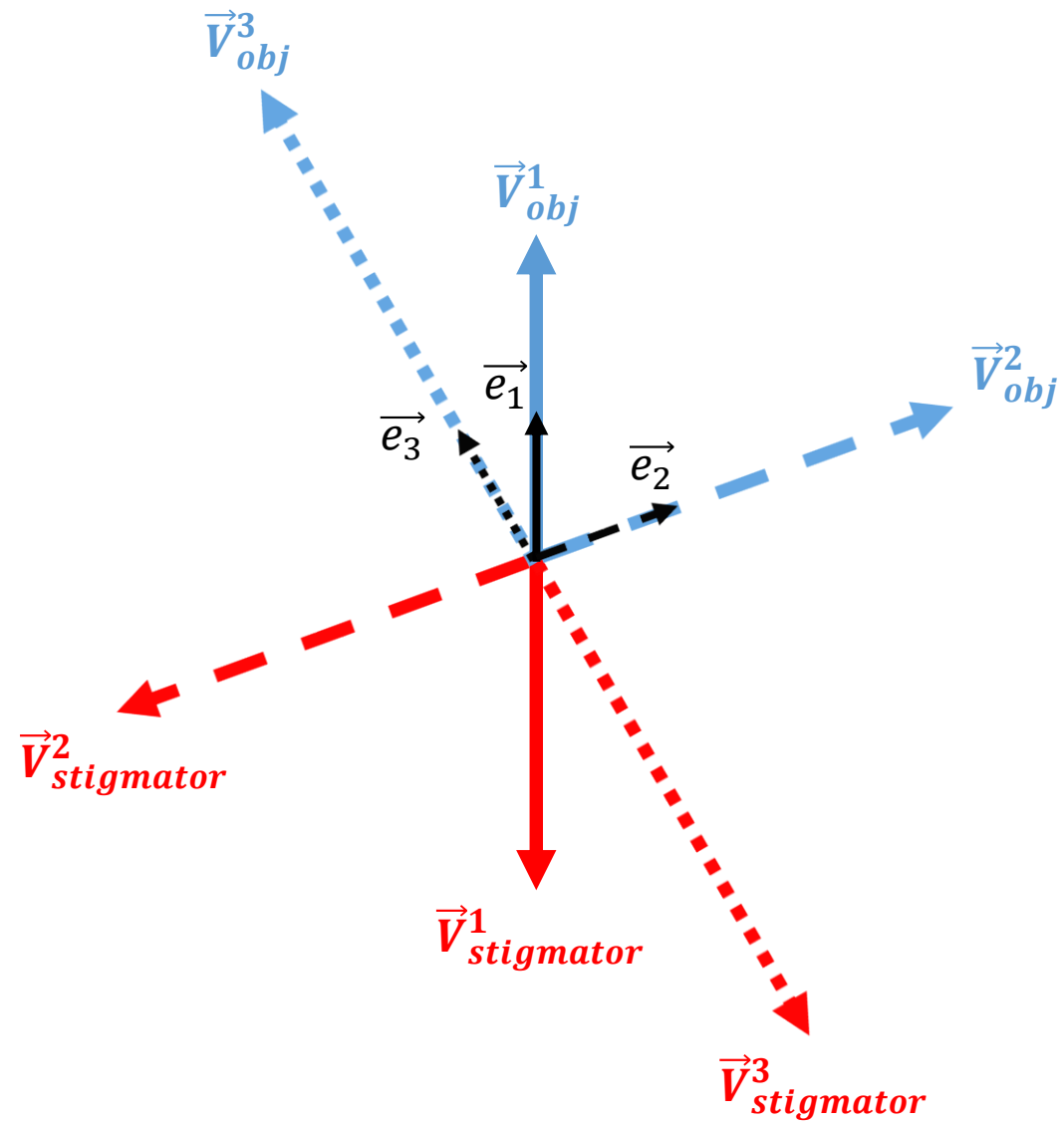


Fig. S1

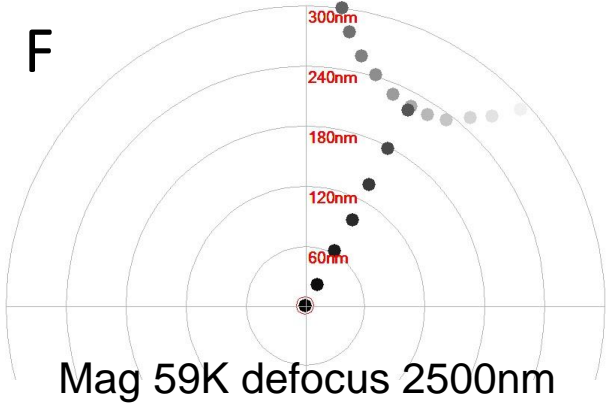
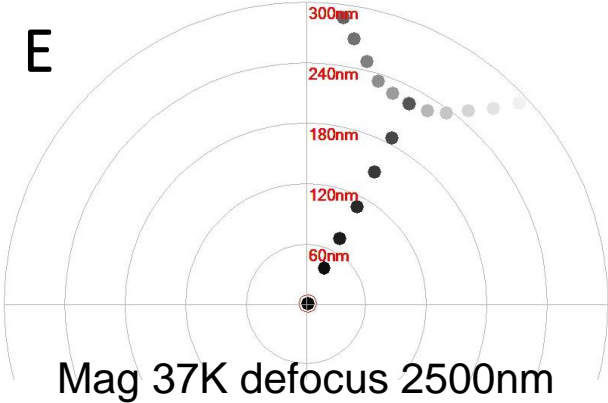
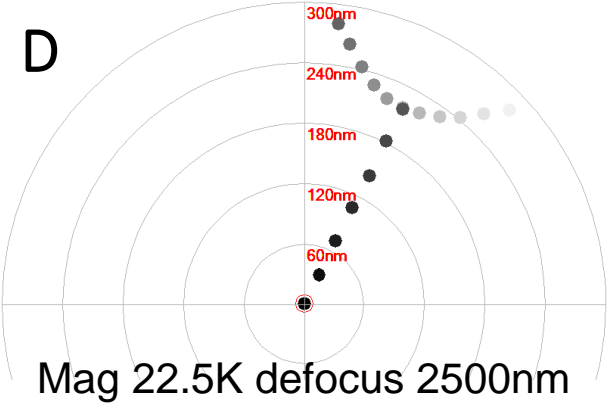
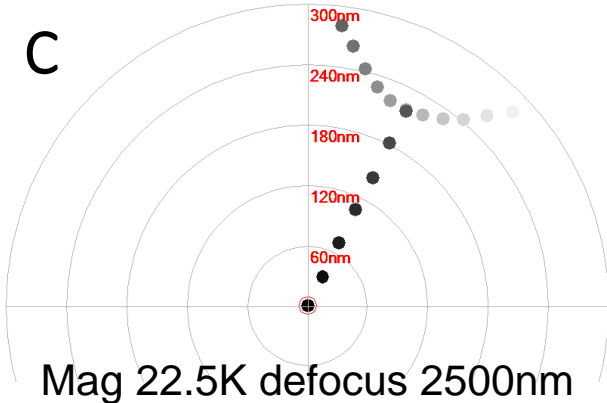
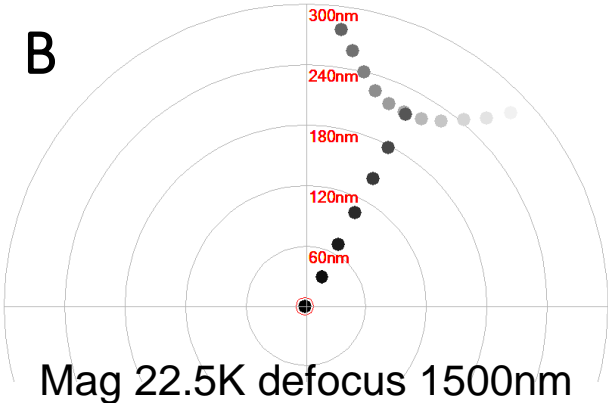
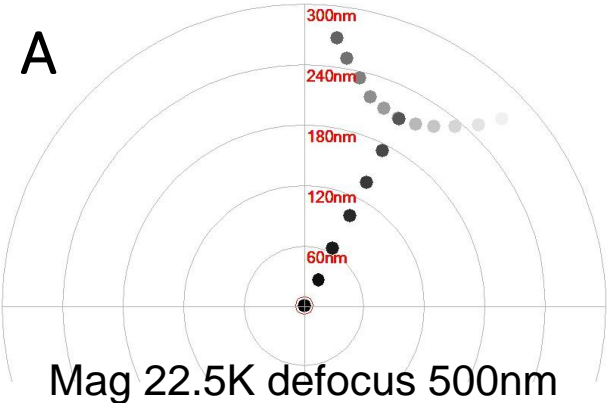


Fig. S2

